Protonation equilibria and pore-opening structure of the dual-histidine influenza B virus M2 transmembrane proton channel from solid-state NMR

Jonathan K. Williams[1\$], Alexander A. Shcherbakov[1], Jun Wang[2] and Mei Hong[1]*

[1] Department of Chemistry, Massachusetts Institute of Technology, Cambridge, MA 02139
[2] Department of Pharmacology and Toxicology, University of Arizona, Tucson, AZ 85721

Running title: *Influenza BM2 proton channel structure from SSNMR*

To whom correspondence should be addressed:

* Mei Hong, Department of Chemistry, Massachusetts Institute of Technology, 170 Albany Street, Cambridge, MA, 02139; Email: meihong@mit.edu; Telephone: (617) 253-5521.

ABSTRACT

The influenza A and B viruses are the primary cause of seasonal flu epidemics. Common to both viruses is the M2 protein, a homo-tetrameric transmembrane (TM) proton channel that acidifies the virion after endocytosis. Although influenza A M2 (AM2) and B M2 (BM2) are functional analogs, they have little sequence homology, except for a conserved HxxxW motif, which is responsible for proton selectivity and channel gating. Importantly, BM2 contains a second titratable histidine, His27, in the TM domain, which forms a reverse WxxxH motif with the gating tryptophan. To understand how His27 affects the proton conduction property of BM2, we have used solid-state NMR (SSNMR) to characterize the pH-dependent structure and dynamics of His27. In cholesterol-containing lipid membranes mimicking the virus envelope, ^{15}N NMR spectra show that the His27 tetrad protonates with higher pK_a's than His19, indicating that the solvent-accessible His27 facilitates proton conduction of the channel by increasing the proton dissociation rates of His19. AM2 is inhibited by the amantadine class of antiviral drugs while BM2 has no known inhibitors. We measured the N-terminal interhelical separation of the BM2 channel using fluorinated Phe5. The interhelical ^{19}F-^{19}F distances show a bimodal distribution of a short distance of 7 Å and a long distance of 15-20 Å, indicating that the phenylene rings do not block small-molecule entry into the channel pore. These results give insights into the lack of amantadine inhibition of BM2 and reveal structural diversities in this family of viral proton channels.

The influenza B virus is a component of seasonal flu infections and becomes prevalent in the spring months (1). Critical to the viral lifecycle is the M2 protein: a single-pass, membrane spanning, homo-tetrameric proton channel responsible for acidifying the virion after endocytosis; acidification of the viral interior initiates uncoating (2). In both influenza A and B M2 proteins, an HxxxW motif is conserved in the TM domain, in which the His is responsible for proton selectivity and acid activation (3,4), while the Trp ensures asymmetric proton conduction from the N-terminus to the C-terminus (5,6). AM2 is inhibited by the amantadine class of antiviral drugs while BM2 has no known inhibitors. The structure and dynamics of AM2 and its drug-resistant mutants have been extensively studied to understand the atomic basis of proton conduction (7-12), channel gating (6,13), and drug inhibition (14-17). In comparison, much less effort has been directed towards studying the BM2 channel (18-20), which has little sequence homology with AM2. Thus, BM2 presents a unique opportunity to understand how different chemical systems perform similar functions. Central to understanding the proton conduction mechanism

of AM2 and BM2 channels are the proton transfer equilibria and dynamics at the conserved HxxxW motif, and how these are affected by the amino acid residues surrounding this motif.

One of the most important sequence differences between BM2 and AM2 channels is the presence of a second histidine, His27, in BM2. This histidine is located three residues C-terminal to Trp23, thus forming a reverse WxxxH motif; the corresponding position in AM2 is a non-titratable Arg45. While mutation of the proton-selective His19 to Cys abolishes proton conduction altogether, as seen in electrophysiological assays on whole cells (21), mutation of His27 to Ala attenuates proton conduction only by ~26% in liposome proton flux assays (19). The mechanism with which His27 influences proton conduction is currently unknown. Recently, using magic-angle-spinning (MAS) SSNMR, we measured the proton-dissociation equilibrium constants (pK$_a$'s) of the His19 tetrad and found them to be one pH unit lower than the pK$_a$'s of the His37 tetrad in AM2 (18). This large pK$_a$ change is surprising, and we hypothesized that the C-terminal His27 may increase the proton dissociation rate of His19, thereby stabilizing the neutral state of His19. If this model were correct, then we would expect His27 to exhibit higher pK$_a$'s than His19.

While high-resolution structures of the AM2 TM domain have been determined using multiple techniques (8,9,11,12,14,16,22), the structure of the BM2 channel has been much less characterized. To date, there is only a single structure of BM2, solved by solution NMR in DHPC micelles (19). The structure shows the channel as a coiled-coil tetramer, with three serine residues (Ser9, Ser12, Ser16) lining the pore and a bulky phenylalanine ring (Phe5) protruding into the pore at the N-terminus. This structure suggests two possible reasons for the inability of amantadine drugs to block BM2: either the polar pore-lining serine residues disfavor binding of the nonpolar drug, or the Phe5 sidechains block drug entry into the channel. Further structural studies of BM2 in lipid bilayers are needed to determine which mechanism is operative, which would help the

development of antiviral drugs against influenza B infections.

SSNMR spectroscopy is a powerful method for elucidating the atomic structures and dynamics of membrane proteins in native-like phospholipid bilayers. Herein, we employ SSNMR to measure the pH-dependent structure and proton-transfer dynamics of His27 and the interhelical separation of the channel at Phe5. The measurements were conducted on BM2(1-33), which has been shown to reproduce the activity of full-length BM2 (19,23). ^{13}C and ^{15}N chemical shifts of His27 as a function of pH revealed the proton dissociation equilibria of the His27 tetrad, while fluorine-tagged Phe5 allowed interhelical separation of the N-terminus to be measured. The data support the hypothesis that His27 siphons protons off His19, while the Phe5 sidechains are spaced too far apart to block small-molecule entry into the BM2 pore.

Results

The BM2 TM domain adopts a pH-independent α-helical conformation

We measured the ^{13}C and ^{15}N chemical shifts of several residues distributed throughout BM2(1-33) to evaluate the backbone conformation as a function of pH. **Figure 1A** shows 2D double-quantum (DQ) and single-quantum (SQ) correlation spectra (called INADEQUATE (24)) of the peptide, measured at pH 5.5 and pH 7.3. With a short dipolar-recoupling time of 0.50 – 0.57 ms for ^{13}C-^{13}C DQ excitation and reconversion, the 2D spectrum exhibits only correlation peaks for directly bonded carbons, thus allowing resonance assignment. Ser9 shows similar Cα and Cβ chemical shifts, characteristic of an α-helical conformation. Similarly, Ile14 (64.1 ppm, 36.0 ppm), Leu18 (55.8 ppm, 40.2 ppm), and Ala22 (53.4 ppm, 17.0 ppm) adopt α-helical Cα and Cβ chemical shifts, which do not change with pH. Thus, the backbone conformation of the BM2 TM domain is independent of pH and is α-helical in the cholesterol-containing membrane, consistent with the result of a previous study using different site-specifically labeled residues (18).

His27 exhibits pH-dependent chemical structures

In contrast to the non-titratable residues, His27 exhibits clear pH-dependent Cα and Cβ chemical shifts. At high pH (**Fig. 1B**), two sets of α-helical Cα and Cβ chemical shifts are observed and can be assigned to the neutral τ (57.8 ppm, 29.1 ppm) and π (56.4, ppm, 25.9 ppm) tautomers through correlation peaks with the sidechain Cγ and Cδ2 (see **Fig. 3** below). At low pH, two sets of Cα-Cβ cross peaks are also resolved, but at lower chemical shifts. These peaks can be assigned to cationic His27 based on their correlations with the Cγ and Cδ2 chemical shifts: the cross peaks at (57.0 ppm, 25.8 ppm) can be assigned to the +4 tetrad (cat4) while the (54.2 ppm, 25.1 ppm) cross peaks can be assigned to the +3 tetrad (cat3).

Figure 2 shows 1D ^{13}C spectra of the His27 sidechain at low temperature where motion and chemical exchange were frozen, and at high temperature where proton-transfer dynamics and reorientational motion can occur. At low temperature, the pH 8.0 and 7.3 spectra are dominated by neutral histidine signals such as the Cδ2 chemical shifts of τ (114.7 ppm) and π (124.2 ppm) tautomers and the Cγ peak of the π tautomer (127.8 ppm). These neutral histidine signals persist down to pH 6.0, below which cationic histidine signals appear: the τ Cδ2 peak broadens due to partial overlap with the cationic Cδ2 peak (~117 ppm); the Cε1 peak broadens and shifts to ~134 ppm; the lipid C=C resonance is partly overlapped by the cationic Cγ peak at ~129 ppm. At pH 5.5, the spectrum is dominated by cationic histidine signals. The high-temperature ^{13}C spectra follow the same trends, except for the Cδ2 peak, which resonates at ~118 ppm at all pH values, indicating that all three species (τ, π, cationic) interconvert to give an average chemical shift (17).

2D ^{15}N-^{13}C correlation spectra (**Fig. 3**) allowed the assignment of the ^{15}N chemical shifts of Nδ1 and Nε2 in the three histidine species. At low pH, only a single ^{15}N chemical shift is observed (~176 ppm) for Nδ1H and Nε2H. At high pH, the τ tautomer is dominant, as seen by the Nε2-Cδ2 (165.2 ppm, 114.7 ppm) and Nδ1-Cγ (248.0 ppm, 138.6 ppm) correlations, while the π tautomer has much lower concentrations, as shown by the low

intensities of the Nδ1H-Cγ (168.1 ppm, 127.8 ppm) and Nε2-Cδ2 (248.0 ppm, 124.2 ppm) cross peaks.

His27 has different proton exchange equilibria from His19

We measured the ^{15}N spectra of His27-labeled BM2(1-33) at six pH values to quantify the proton-dissociation constants. For the tetrameric channel, His27 can be treated as a tetraprotic acid, with a maximum of four proton-dissociation constants. As shown before, the ratio of the protonated and unprotonated ^{15}N intensities, I_{NH}/I_N, can be used to extract the pK$_a$'s (25). **Figure 4A** shows low-temperature ^{15}N spectra as a function of pH. The 250-ppm ^{15}N peak results from unprotonated imidazole nitrogen while the 170-ppm peak is due to protonated nitrogens. At high pH, a relatively sharp ^{15}N peak at ~167 ppm is detected and can be assigned to τ tautomer Nε2H and π tautomer Nδ1H. At the intermediate pH of 6.0, both neutral and cationic NH peaks are observed, while below pH 6.0 only cationic NH signals are observed. As expected, the 250-ppm intensity decreases progressively from high to low pH, giving a high [His]/[HisH$^+$] ratio of 7.7 at pH 8.0 but a low ratio of 0.09 at pH 5.5 (**Fig. 5A, B, Table 1**). Fitting these histidine concentration ratios yielded four pK$_a$'s of 7.9 ± 0.01, 5.9 ± 0.01, 5.9 ± 0.01, and 5.8 ± 0.01. Thus, the His27 tetrad already acquires a +1 charge at about pH 8, and the +1 charge persists to about pH 5.9, when the other three His27 residues rapidly protonate to reach the fully charged +4 tetrad (**Fig. 5C**).

At high temperature, the His27 imidazole ^{15}N spectra show extensive chemical exchange, with strong intensities at averaged chemical shifts of 170–250 ppm (**Fig. 4B**). In stark contrast to the proton-selective His19 in BM2 and His37 in AM2, the exchange intensities of His27 are visible already at pH 8 and pH 7.3, where His19 and His37 show no exchange averaging. Moreover, the His27 exchange band is much broader than His19 and His37, indicating a broad distribution of equilibrium constants. As the pH lowers, both the exchange intensities and the exchange linewidths decrease, consistent with the decreasing neutral histidine population, which reduces the fraction of

3

histidines undergoing exchange. A relatively narrow exchange peak is observed at 188 ppm and was previously assigned to Nε2 exchange among τ, π, and cationic histidine (17), indicating that the exchange populations are similar between His27 and His19.

Phe5 interhelical distances are large at both low and high pH

We measured interhelical ^{19}F-^{19}F distances between 4-^{19}F-Phe5 using the centerband-only detection of exchange (CODEX) experiment (26,27). Representative control (S_0, black) and dephased (*S*, red) spectra at a mixing time of 500 ms are shown in **Fig. 6A** for the pH 5.5 and pH 8.0 samples. Although the S/S_0 ratio of the isotropic peak (centerband) is smaller for the low-pH sample than the high-pH sample, when the sideband intensities are taken into account, the average S/S_0 values are similar between the two. **Fig. 6b** shows the full CODEX decay curves, with final S/S_0 values of 0.41 ± 0.10 at pH 5.5 and 0.45 ± 0.10 at pH 8.0, measured at a mixing time of 2 s. Longer mixing times could not be measured as T_1 relaxation causes prohibitively low sensitivity.

The measured CODEX decays show an initial fast decay and a slower decay at longer mixing times, indicating a distribution of inter-fluorine distances. Consistently, simulations assuming a symmetric 4-spin system (i.e. a square model) did not fit the data well (**Fig. 6B**). A dimer model involving only two spins also does not fit the data, since the observed final S/S_0 intensities are well below the value of 0.5 expected for a dimer. The data thus indicate an asymmetric 4-spin geometry, which can be either a rectangular geometry or a combination of two square geometries. For the rectangular model, assuming a Gaussian distribution with a standard deviation of 1 Å for each distance component, we found a best fit with two nearest-neighbor distances of 7 Å and 15 Å at both pH (**Fig. 6C**). Here the longer distance is a lower bound, since the root-mean-square deviation (RMSD) between the simulated and experimental CODEX curves are insensitive to the longer distance up to 20 Å, reflecting the well-known low precision of measuring weak dipolar couplings. For the model of two square geometries, a mixture

of 60% of a square with a side length of 7.0 Å and 40% of a square with a side length of 15.3 Å gave the best fit to the experimental data (**Fig. 6E**). However, this scenario of a sharp bimodal distribution of two Phe5 conformations to generate two very different interhelical distances is unlikely, since only a single ^{19}F chemical shift is observed for Phe5, and the ^{13}C chemical shifts of non-titratable residues in the peptide also do not exhibit multiplicity. The ^{19}F chemical shifts are highly sensitive to the local environment, thus the presence of two distinct populations of square geometries would be expected to give rise to two ^{19}F peaks, which is not observed. Therefore, the rectangular model is the more likely reason for the biexponential decay of the CODEX intensities.

Based on the solution NMR backbone structure (19) (PDB: 2KIX), we varied the χ_1 torsion angle of Phe5 to satisfy the measured inter-helical ^{19}F-^{19}F distances. Two χ_1 angles of +60° and -60°, placed on neighboring helices, reproduced the experimental data, with inter-^{19}F Phe5-Phe5 distances of ~7.5 Å for the short sides and ~19.5 Å for the long sides (**Fig. 6D**), which fall within the minimum RMSD valley (**Fig. 6C**). For comparison, the χ_1 angles that satisfy the bimodal square model are ~140° (*t*) for the 7.5 Å distance and either 60° (*p*) or -60° (*m*) for a ~14.5 Å nearest-neighbor distance.

Discussion

The current data show similarities as well as important differences between His27 in the reverse WxxxH motif and His19 in the HxxxW motif of BM2 (18). First, the ^{13}C and ^{15}N chemical shifts of the His27 imidazole, in composite, are similar to the chemical shifts of His19 in BM2 and His37 in AM2, as dictated by the chemical structures of histidine. The His27 tetrad shows coexistence of the +3 and +4 charge states at low pH, also similar to His19 (18) and H37 in AM2 (7,25) (**Fig. 5C**). However, in contrast to the proton-selective histidines in BM2 and AM2, the pH at which cationic His27 dominates and neutral His27 diminishes is much higher for the solvent-exposed His27 tetrad. The transition occurs at about pH 6, the inflection point of the titration curve (**Fig. 5B**). Specifically, the unprotonated ^{15}N signal has disappeared at pH 5.5 for His27 while it persists

down to pH 4.5 for His19 (18). The titration behavior of His27 partly resembles amino acid histidine in solution, which has a pK_a of 6.1 (28), suggesting that His27 is sufficiently solvent-accessible that it protonates similarly to free histidine in solution. However, the His27 tetrad differs from free histidine in that it has a high first pK_a of 7.9; in other words, the His27 tetrad already harbors +1 charge at neutral pH. Most importantly, these data indicate that His27 protonates at about 1 pH unit higher (average pK_a = 6.4) than His19 (average pK_a = 5.1). A previous study measuring pH-dependent Trp fluorescence emission spectra, UV resonance Raman spectra, circular dichroism spectra, and proton conductance of wild-type and H19A and H27A mutants of BM2, identified a pK_a of ~7.6 for His27 and ~6.5 for His19 (20). The current SSNMR data of His27 supports the previous conclusion and adds further quantitative information about the three acidic pK_a's. The previous study used POPE/POPS (1 : 1) liposomes, where the negatively charged POPS lipids are expected to favor proton association to both histidines and thus elevate the pK_a's.

The fact that His27 is protonated at higher pH than His19 supports the model that it can siphon off protons from His19, stabilizing neutral His19 and depressing its pK_a's. In this way, His27 can facilitate proton release from the HxxxW dyad and increase the proton conduction to the C-terminus, which is consistent with the mutagenesis result that H27A mutation decreases the channel activity (19,20).

The ^{19}F CODEX data of 4-^{19}F-Phe5 revealed unexpected asymmetry in the oligomeric assembly of the N-terminus of the BM2 channel. The solution NMR structure of DHPC-micelle bound BM2(1-33) (19) shows the Phe5 sidechain to point into the pore, with a χ_1 angle of ~180°. This conformation suggests that the Phe5 sidechain may obstruct the pore, which may partly explain the inability of amantadine drugs to bind BM2 (14,15). The current ^{19}F distance data rule out this model. The CODEX decay curves at both high and low pH fit well to a rectangular geometry with a short distance of 7±1 Å and a long distance of 15 – 20 Å. Both distances are too large to block the pore. Therefore, these data imply that the lack of

binding of hydrophobic adamantane drugs to BM2 results from the polar character of the channel, with three serine residues lining the pore (2,19,21).

The asymmetric interhelical distances found in the Phe5 ^{19}F CODEX data differ qualitatively from the CODEX result of 5-^{19}F-Trp41 in AM2, which show a single nearest-neighbor distance of 11-12 Å, indicating a C4-symmetric square geometry (13,29). Interestingly, distance asymmetry was also previously observed at Val27 in AM2. When V27 was mutated to 4-^{19}F-Phe, the ^{19}F CODEX data showed a bimodal decay that corresponds to an equimolar mixture of a 5.3 Å distance and a 12.3 Å distance (29). The fact that both AM2 and BM2 channels show asymmetric interhelical separations at the N-terminus is intriguing, but the reason for this asymmetry is unclear at present. Since no chemical shift multiplicity was observed for the non-titratable residues in these samples, the structural heterogeneity more likely occurs in the sidechains rather than the backbone. The near terminal location of Phe5 in BM2 and V27F in AM2 makes it possible for these sidechains to adopt flexible χ_1 torsion angles. However, Trp41 is also located near the C-terminus of the TM domain but does not exhibit such an asymmetry. Another possibility is that the 4-^{19}F-Phe tag may cause perturbation to the helix bundle, but the lack of distance asymmetry for the 5-^{19}F-Trp tag of the indole ring also disfavors this scenario. Future studies using ^{13}C, ^{15}N-labeled recombinant protein samples will be useful for determining whether there is functionally important sidechain asymmetry and the high-resolution structure of BM2 in lipid bilayers.

Conclusions

The present SSNMR data give new insights into atomic-level structural and dynamical details of proton conduction through the BM2 channel and the lack of amantadine inhibition of this protein. The pK_a's of His27 tetrad are found to be 7.9, 5.9, 5.9, and 5.8. Thus, the C-terminal His27 has much higher pK_a's than the interior, proton-selective His19, explaining the stabilization of neutral His19 compared to His37 in the influenza A M2 channel. We conclude that His27 speeds up proton dissociation from the HxxxW motif, thus facilitating proton conduction by BM2.

Interhelical ^{19}F-^{19}F distance measurements indicate that Phe5 sidechains at the N-terminus of the TM domain are separated by 7 Å and 15-20 Å from each other, thus this residue does not block small molecules from entering the channel pore. Design of BM2 inhibitors should therefore target the polar pore-lining surface of the BM2 channel.

Experimental Procedures
Synthesis of BM2(1-33) peptides
The TM domain (residues 1-33: MLEPFQILS ISSFILSALH FMAWTIGHLN QIKR) of the B/Maryland/1/2001 strain of the influenza virus was synthesized using Fmoc chemistry as described previously (15,17,18). Uniformly $^{13}C,^{15}N$-labeled amino acids (Sigma-Aldrich and Cambridge Isotope Laboratories) were incorporated at Ser9, Ile14, Leu18, Ala22, and His27. 4-^{19}F-phenylalanine (Sigma-Aldrich) was incorporated at Phe5.

Membrane sample preparation
Isotopically labeled BM2(1-33) peptide was reconstituted into a virus-mimetic (VM+) membrane, consisting of 1-palmitoyl-2-oleoyl-*sn*-glycero-3-phosphocholine (POPC), 1-palmitoyl-2-oleoyl-*sn*-glycero-3-phosphoethanolamine (POPE), Sphingomyelin (SPM), and cholesterol at molar fractions of 25.6%, 25.6%, 25.6%, and 23.1%, respectively. The peptide : lipid molar ratio was 1 : 13.3. The lipids were codissolved in chloroform and methanol, while the peptide was dissolved in ~500 μL of 2,2,2-trifluoroethanol (TFE). Nitrogen gas was used to concentrate the lipid solution to ~1 mL, then added to the peptide/TFE solution. The solvent was removed under nitrogen gas and placed under room temperature vacuum overnight. The dried lipid/peptide mixture was then lyophilized for 3+ hours to fully remove residual TFE and TFA. The dried lipid/peptide powder was resuspended in 3 mL of the desired buffer and vortexed for 2 hours, followed by 8 freeze-thaw cycles between liquid nitrogen and a 35°C water bath to create large multilamellar vesicles. The membrane pellets were collected by ultracentrifugation at 50,000 rpm at 4°C for 4 hours, and allowed to dry slowly to 40wt% water in a desiccator. The proteoliposome mixture was spun into 4 mm or 3.2 mm magic-angle spinning (MAS) rotors for solid-state NMR experiments.

Control of sample pH was crucial for accurate determination of the His27 pK_a's. The pH was measured at several stages during membrane sample preparation: during the initial buffer preparation, immediately before addition of buffer to the lyophilized peptide/lipid mixture, after vortexing the mixture with buffer for two hours, and a final check of the supernatant after ultracentrifugation. Reported pH values and errors are the average and standard deviation of these measurements. In cases where the pH of the lipid/peptide mixture deviated by up to 0.3 pH units from the pH of the original buffer, the mixture was dialyzed against 1 L of the original buffer overnight using 1 kDa MWCO dialysis tubing prior to centrifugation. A total of six samples at different pH values were prepared using the following buffers: pH 5.5 ± 0.1 (10 mM citric acid/citrate, 1 mM EDTA, 0.1 mM NaN_3), pH 5.70 ± 0.04 (30 mM citric acid/citrate, 3 mM EDTA, 0.3 mM NaN_3), pH 6.0 ± 0.1 (20 mM Bis-Tris/HCl, 1 mM EDTA, 0.1 mM NaN_3), pH 6.4 ± 0.1 (10 mM Bis-Tris/HCl, 1 mM EDTA, 0.1 mM NaN_3), pH 7.3 ± 0.3 (10 mM Tris/HCl, 1 mM EDTA, 0.1 mM NaN_3), pH 8.0 ± 0.1 (10 mM Tris/HCl, 1 mM EDTA, 0.1 mM NaN_3).

Solid-state NMR experiments
SSNMR experiments were carried out on Bruker Avance 400 MHz (9.4 T), 600 MHz (14.1 T), and 800 MHz (18.8 T) spectrometers using 4 mm or 3.2 mm $^1H/^{13}C/^{15}N$ or $^1H/^{19}F/^{13}C$ MAS probes. Typical radiofrequency (rf) field strengths were 71–100 kHz for ^1H, 55–71 kHz for ^{13}C, 35–45 kHz for ^{15}N, and 62–71 kHz for ^{19}F. Chemical shifts were externally referenced to the CH_2 signal of adamantane at 38.48 ppm on the tetramethylsilane (TMS) scale for ^{13}C, the amide signal of N-acetylvaline at 122.0 ppm on the liquid ammonia scale for ^{15}N, and the Teflon signal at -122.0 ppm for ^{19}F.

1D ^{13}C and ^{15}N cross-polarization (CP) MAS spectra were measured between 243 K and 313 K. ^{13}C CP experiments were measured at 9.4 T under 7-9 kHz MAS or at 18.8 T under 14.5 kHz MAS. A 90–100% ramp was applied to the ^{13}C channel during a 1 ms ^1H–^{13}C spin lock. The ^{15}N CP

experiments were conducted at 9.4 T under 7 kHz MAS using a ^1H–^{15}N spin lock of 3 ms. To obtain adequate signal-to-noise ratios (SNR), 40,000 to 100,000 scans were averaged for the ^{15}N spectra. ^{15}N CP signal intensities were used to quantify the relative populations of protonated (~170 ppm) and unprotonated (~250 ppm) nitrogens in the His27 sidechain. To correct for differences in polarization transfer between the protonated and unprotonated nitrogens, the ^1H–^{15}N CP matching condition was optimized on a pH 8.5 histidine model compound (30) to maximize the intensity of the unprotonated ^{15}N peak. The ratio of the integrated intensities between the protonated and unprotonated regions of this model compound, ranging from 1.27 to 1.58, was used as a correction factor for the unprotonated nitrogen signal intensity on BM2 samples when extracting the ratio of neutral to cationic His27.

2D ^{13}C–^{13}C correlation spectra were measured using 100 ms of dipolar-assisted rotational resonance (DARR) (31) mixing. 2D double quantum (DQ) INADEQUATE spectra were measured at 14.1 T and 243 K, under 7 or 8 kHz MAS (24). The SPC5 (32) sequence was used for ^{13}C–^{13}C dipolar recoupling and DQ excitation and reconversion. 2D ^{15}N-^{13}C correlation spectra were measured at 9.4 T and 243 K under 9 kHz MAS, using a REDOR pulse sequence (33) with mixing times of 0.3-0.6 ms.

^{19}F CODEX (26) spectra were measured at 9.4 T and 235 K under 10 kHz MAS. The control (S_0) and dephased (S) spectra were acquired within an hour of each other to minimize changes in the experimental conditions over time. In the S experiments, the exchange mixing times (τ_m) were 50, 100, 200, 500, 1000, and 2000 ms, while the z-filter time (τ_z) was kept constant at 1 ms. The S_0 experiments used the reverse, where τ_m was fixed at 1 ms while τ_z varied between 50 ms and 2000 ms. To obtain adequate SNR, 9,000 – 32,000 scans were averaged. Uncertainties of the S/S_0 values were propagated from the SNR of the spectra.

Extraction of His27 pK$_a$ values

Conflict of Interest

His27 proton-dissociation constants were extracted from the ^{15}N CP spectra as described before (18,25). In brief, the signals of protonated and unprotonated His27 side-chain ^{15}N atoms were integrated from 200–150 ppm and 265–236 ppm, respectively. The integration for the unprotonated nitrogen signal is multiplied by an experimentally measured correction factor, κ, which represents the lower CP efficiency of this atom. The neutral-to-cationic histidine ratio was calculated using:

$$\frac{[His]}{[HisH^+]} = 2\left[\frac{(I_{NH}/I_N)}{\kappa} - 1\right]^{-1}.$$

The neutral-to-cationic histidine ratios were fit to the following equation to extract the His27 tetrad pK$_a$'s:

$$\frac{[His]}{[HisH^+]} = \frac{1 \cdot \frac{K_{a1}}{10^{-pH}} + 2 \cdot \frac{K_{a1} \cdot K_{a2}}{10^{-2pH}} + 3 \cdot \frac{K_{a1} \cdot K_{a2} \cdot K_{a3}}{10^{-3pH}} + 4 \cdot \frac{K_{a1} \cdot K_{a2} \cdot K_{a3} \cdot K_{a4}}{10^{-4pH}}}{4 + 3 \cdot \frac{K_{a1}}{10^{-pH}} + 2 \cdot \frac{K_{a1} \cdot K_{a2}}{10^{-2pH}} + 1 \cdot \frac{K_{a1} \cdot K_{a2} \cdot K_{a3}}{10^{-3pH}}}$$

Simulation of ^{19}F CODEX curves and distance extraction

CODEX magnetization exchange curves were calculated using an exchange-matrix formalism for a four-spin system (34). The exchange rate constants are proportional to an overlap integral $F(0)$ and the square of the ^{19}F dipolar coupling constants, which depend on the F-F distances in the tetramer. An $F(0)$ value of 41 μs was used, determined from model-compound experiments at 10 kHz MAS. The dephasing curves for rectangular geometries with side lengths of 2-25 Å in 0.1 Å increments were calculated. The simulated curves were multiplied by Gaussian weights with a standard deviation of 1 Å and summed together to generate dephasing curves representing a weighted population of distances. The reported best-fit distance corresponds to the center of the Gaussian distribution. The best-fit simulation was obtained from the minimal RMSD between the calculated dephasing curves and the experimental curve.

The authors declare that they have no conflicts of interest with the contents of this article.

Author Contributions

MH and JKW designed the study. JW synthesized the peptides. JKW and AAS prepared the samples and performed the NMR experiments. JKW, AAS, and MH analyzed the data and wrote the manuscript. All authors reviewed the results, edited and approved the final version of the manuscript.

References
FOOTNOTES

[$]Present address: Department of Chemistry & Chemical Biology, Rutgers University, Piscataway, NJ 08854

Abbreviations:
Fmoc, fluorenylmethyloxycarbonyl; VM+, eukaryotic-mimetic membrane; POPC, 1-palmitoyl-2-oleoyl-*sn*-glycero-3-phosphocholine; POPE, 1-palmitoyl-2-oleoyl-*sn*-glycero-3-phosphoethanolamine; SPM, sphingomyelin; TFE, 2,2,2-trifluoroethanol; MAS, magic-angle spinning; SSNMR, solid-state NMR; MWCO, molecular weight cutoff; TMS, tetramethylsilane; CP, cross polarization; HETCOR, heteronuclear correlation; REDOR, rotational-echo double-resonance; PDSD, proton-driven spin-diffusion; DARR, dipolar-assisted rotational resonance; INADEQUATE, incredible natural abundance double quantum transfer experiment; CODEX, centerband-only detection of exchange; DQ, double quantum; SNR, signal to noise ratio; FWHM, full-width half-maximum; RMSD, root-mean-square deviation.

Table 1. pH-dependent His27 ^{15}N peak intensities and neutral-to-cationic histidine concentration ratios.

pH	I_{NH}/I_N	κ	[His]/[HisH$^+$]
5.5 ± 0.1	35 ± 10	1.47 ± 0.09	0.09 ± 0.03
5.70 ± 0.04	18 ± 8	1.33 ± 0.06	0.16 ± 0.07
6.0 ± 0.1	2.7 ± 0.5	1.47 ± 0.09	2.4 ± 0.5
6.4 ± 0.1	2.4 ± 0.3	1.41 ± 0.08	2.9 ± 0.4
7.3 ± 0.3	2.1 ± 0.1	1.6 ± 0.1	6.4 ± 0.5
8.0 ± 0.1	1.6 ± 0.1	1.27 ± 0.04	7.7 ± 0.5
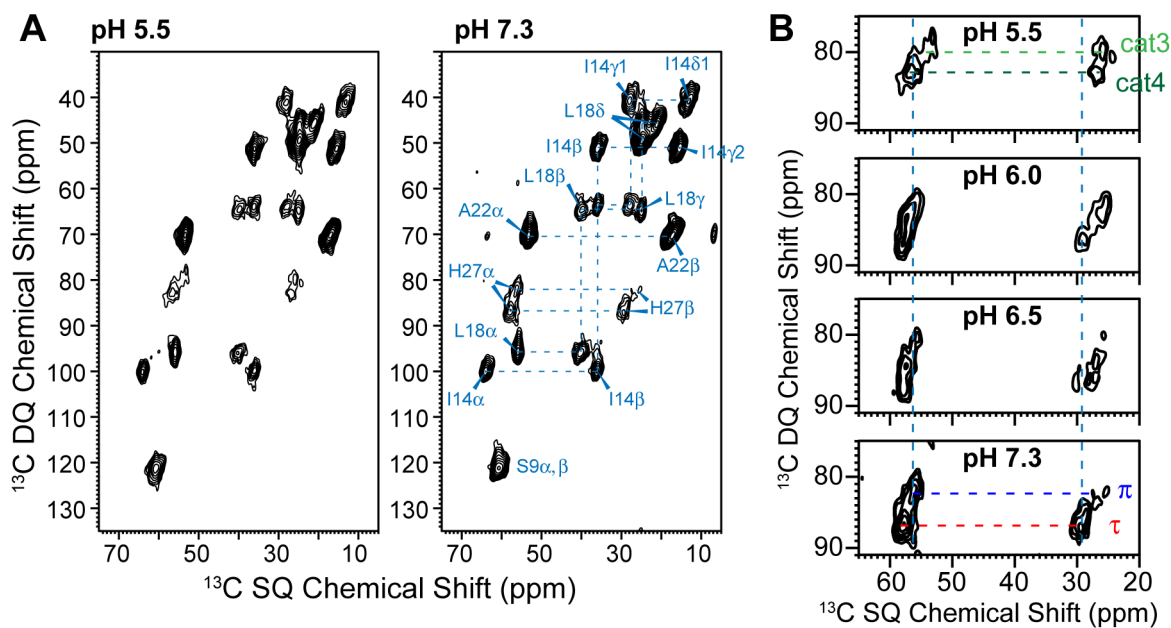
FIGURE 1. 2D ^{13}C-^{13}C INADEQUATE spectra of membrane-bound BM2(1-33) measured at 243 K. (A) 2D spectra at pH 5.5 and pH 7.3. (B) His27 chemical shifts as a function of pH. The Ser9, Ile14, Leu18 and Ala22 chemical shifts are insensitive to pH, while His27 shows pH-dependent changes of Cα and Cβ chemical shifts.
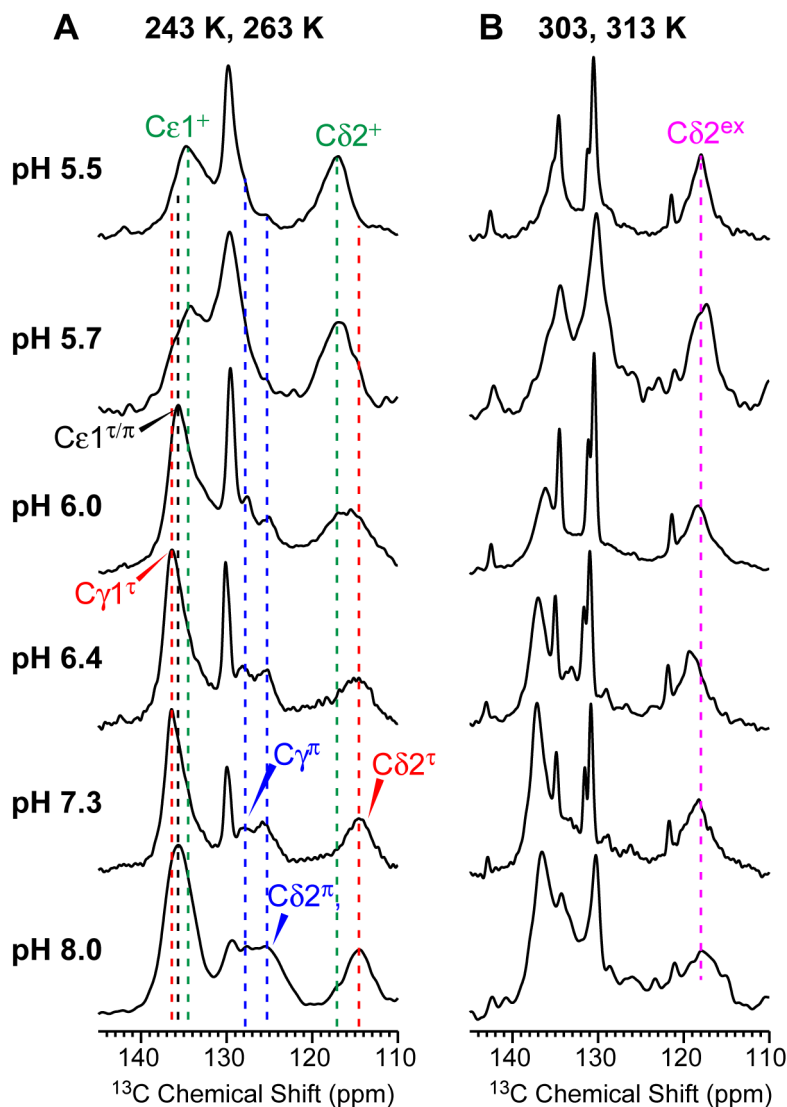
FIGURE 2. ^{13}C CP-MAS spectra of His27 in VM+ membrane-bound BM2(1-33) as a function of pH. The spectra were measured at (A) 243 or 263 K and (B) 303-313 K, under 7-14.5 kHz MAS. At low temperature, the Cδ2 chemical shift differs significantly between low and high pH, with cationic histidine (~117 ppm, +) present at low pH and neutral tautomers (~114 ppm, τ) present at high pH. At high temperature, a Cδ2 exchange peak is observed at ~118 ppm, indicating interconversion among all three histidine species.
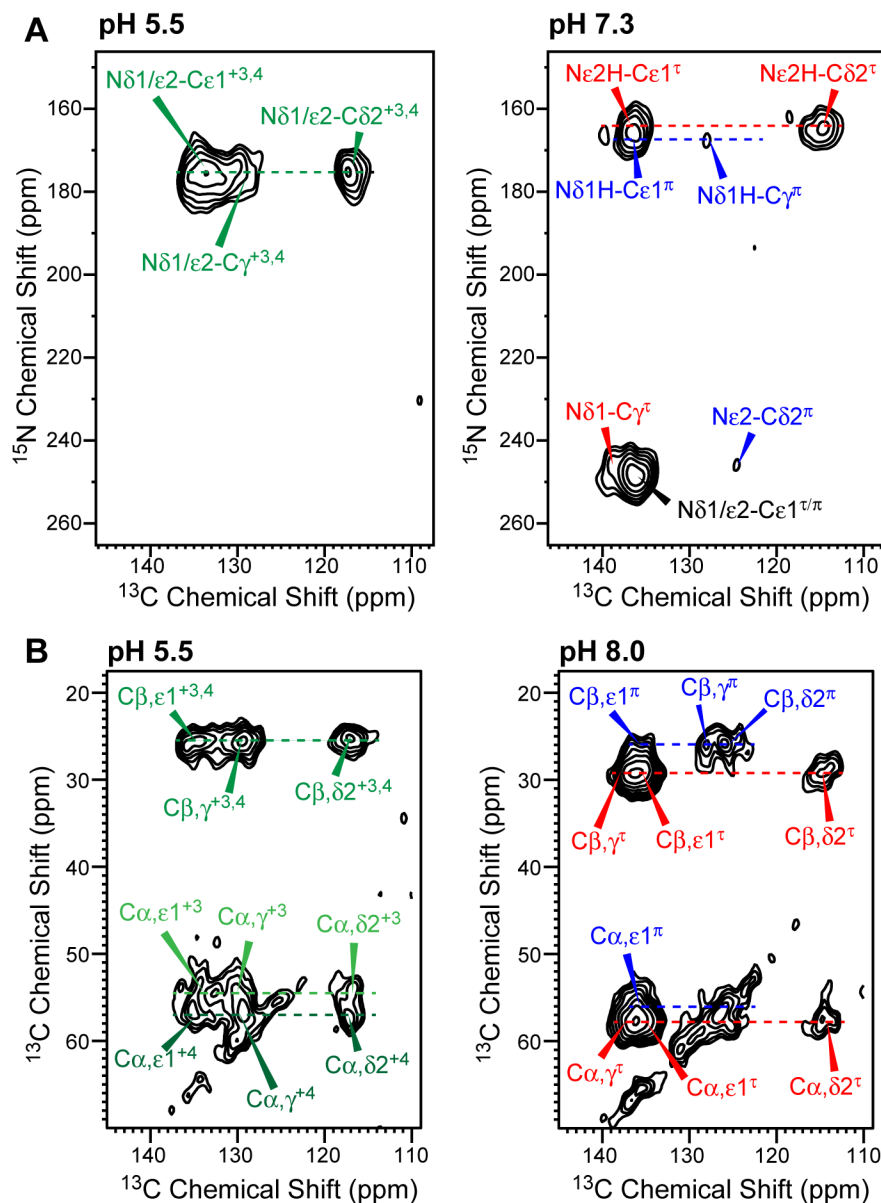
FIGURE 3. 2D ^{15}N-^{13}C and ^{13}C-^{13}C correlation spectra of His27 sidechain in membrane-bound BM2(1-33). (A) The ^{15}N-^{13}C spectra were measured at 243 K under 9 kHz MAS, using ^{15}N-^{13}C REDOR mixing times of 0.3-0.6 ms. At high pH mainly τ tautomer cross peaks (red), Nε2H-Cδ2 and Nδ1-Cγ, are observed. The π tautomer (blue) ^{15}Nδ1H chemical shift largely overlaps with the τ ^{15}Nε2H peak, but can be assigned based on the weak cross peaks with π ^{13}Cγ (~126 ppm) and ^{13}Cδ2 (~124 ppm). (B) The ^{13}C-^{13}C spectra were measured at 243 K under 7 kHz MAS, using a DARR mixing time of 100 ms. The Cβ correlation peaks allow assignment of cat3 and cat4 states at low pH and unambiguous assignment of the neutral τ and π tautomers at high pH.
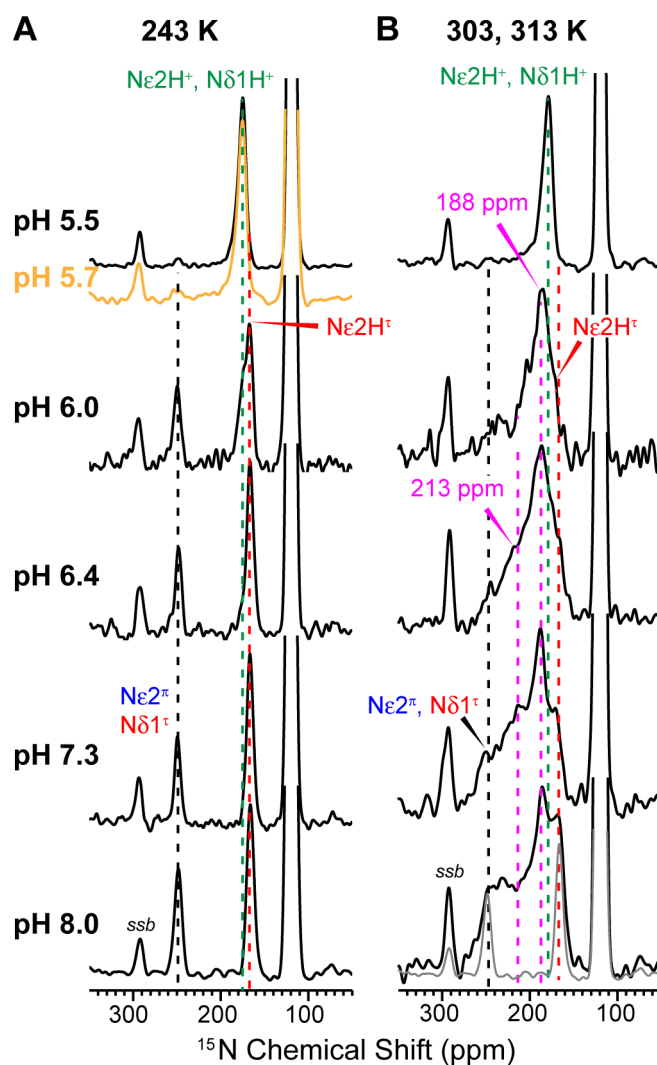
FIGURE 4. [15]N CP-MAS spectra of the His27 sidechain as a function of pH, measured at (A) 243 K and (B) 303 K or 313 K. (a) The non-protonated (~250 ppm) ^{15}N peak shows the expected intensity decrease with decreasing pH, indicating higher populations of cationic His27. The chemical shifts of [15]Nε2 and [15]Nδ1 of the neutral τ and π tautomers are indistinguishable, in contrast to previous observations of His19 in BM2 and His37 in AM2. (b) At high temperature, the spectra show broad exchange peak intensities at 170-250 ppm. The 290-ppm peak seen in all spectra is a spinning sideband (ssb) of backbone amide [15]N.
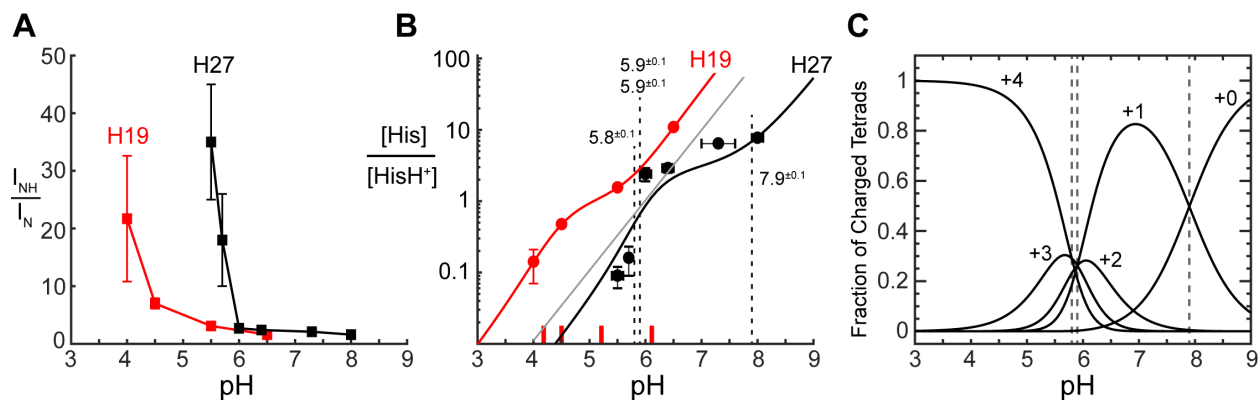
FIGURE 5. Determination of His27 tetrad pK_a's from the imidazole ^{15}N spectra. (A) Relative intensities of protonated (I_{NH}) and non-protonated (I_N) imidazole nitrogens as a function of pH. (B) Ratio of neutral to cationic histidine concentrations as a function of pH. His27 data (*black*) is compared with previously measured His19 (*red*) data (18). The grey line is the best fit of the H27 data assuming a single pK_a for all four histidines. This model does not fit the data well. (C) Populations of charged His27 tetrads as a function of pH. The intercepts between adjacent charge states correspond to the specific pK_a's.
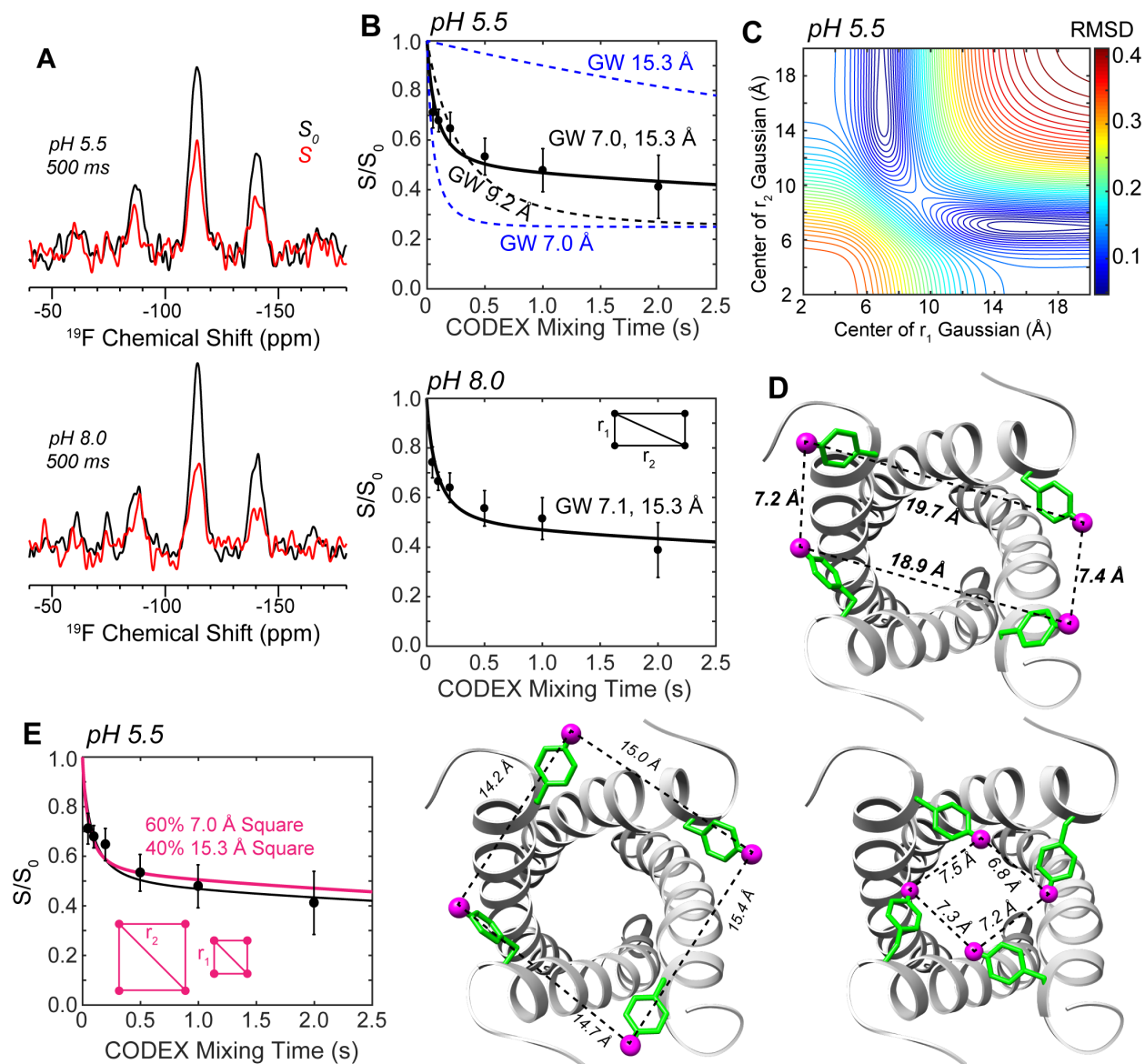
FIGURE 6. ^{19}F CODEX data of 4-^{19}F-Phe5 labeled BM2(1-33) for determining interhelical distances at the N-terminal opening of the tetramer. (A) Representative CODEX spectra measured at 235 K under 10 kHz MAS. The control (S_0, *black*) and dephased (S, *red*) spectra at pH 5.5 and pH 8.0 were measured at a mixing time of 500 ms. (B) Normalized CODEX intensities (S/S_0) as a function of mixing time. The high and low pH samples show similar dephasing, indicating similar interhelical separations. Black dashed curve is the best-fit assuming a square geometry, while blue curves show the two distances that provide the best-fit assuming a rectangular geometry. All distance components are Gaussian-weighted (GW). (C) RMSD between simulated rectangular-geometry CODEX curves as a function of distances (r_1, r_2) and the measured pH 5.5 data, (D) Structural model using the PDB 2KIX backbone, showing Phe5 with χ_1 angles of +65º, -65º, +60º, -60º, which forms a rectangle geometry that satisfies the measured distances. (E) Simulated CODEX curve (magenta) for a weighted average of two square geometries, overlaid with the best-fit rectangular-geometry dephasing curve. The long-distance component is satisfied by a Phe5 χ_1 angle of -45˚ while the short-distance component is satisfied using a χ_1 angle of -135º to -145.

References

1. Koutsakos, M., Nguyen, T., Barclay, W., and Kedzierska, K. (2016) Knowns and Unknowns of Influenza B Viruses. *Future Microbiol*. 11, 119-135
2. Pinto, L., and Lamb, R. (2006) The M2 Proton Channels of Influenza A and B Viruses. *J. Biol. Chem*. 281, 8997-9000
3. Pinto, L., Dieckmann, G., Gandhi, C., Papworth, C., Braman, J., Shaughnessy, M., Lear, J., Lamb, R., and DeGrado, W. (1997) A Functionally Defined Model for the M2 Proton Channel of Influenza A Virus Suggests a Mechanism for its Ion Selectivity. *Proc. Natl. Acad. Sci. U.S.A*. 94, 11301-11306
4. Betakova, T., and Kollerova, E. (2006) pH Modulating Activity of Ion Channels of Influenza A, B, and C Viruses. *Acta Virol*. 50, 187-193
5. Mandala, V., Liao, S., Kwon, B., and Hong, M. (2017) Structural Basis for Asymmetric Conductance of the Influenza M2 Proton Channel Investigated by Solid-State NMR Spectroscopy. *J. Mol. Biol*. 429, 2192-2210
6. Tang, Y., Zaitseva, F., Lamb, R., and Pinto, L. (2002) The Gate of the Influenza Virus M2 Proton Channel is Formed by a Single Tryptophan Residue. *J. Biol. Chem*. 277, 39880-39886
7. Liao, S., Yang, Y., Tietze, D., and Hong, M. (2015) The Influenza M2 Cytoplasmic Tail Changes the Proton-Exchange Equilibria and the Backbone Conformation of the Transmembrane Histidine Residue to Facilitate Proton Conduction. *J. Am. Chem. Soc*. 137, 6067-6077
8. Acharya, A., Carnevale, V., Fiorin, G., Levine, B. G., Polishchuk, A., Balannick, V., Samish, I., Lamb, R. A., Pinto, L. H., DeGrado, W. F., and Klein, M. L. (2010) Structural Mechanism of Proton Transport Through the Influenza A M2 Protein. *Proc. Natl. Acad. Sci. U.S.A*. 107, 15075-15080
9. Andreas, L. B., Reese, M., Eddy, M. T., Gelev, V., Ni, Q. Z., Miller, E. A., Emsley, L., Pintacuda, G., Chou, J. J., and Griffin, R. G. (2015) Structure and Mechanism of the Influenza A M218-60 Dimer of Dimers. *J. Am. Chem. Soc*. 137, 14877-14886
10. Hu, F., Luo, W., and Hong, M. (2010) Mechanisms of Proton Conduction and Gating in Influenza M2 Proton Channels from Solid-State NMR. *Science* 330, 505-508
11. Sharma, M., Yi, M., Dong, H., Qin, H., Peterson, E., Busath, D., Zhou, H. X., and Cross, T. A. (2010) Insight into the Mechanism of the Influenza A Proton Channel from a Structure in a Lipid Bilayer. *Science* 330, 509-512
12. Thomaston, J. L., Alfonso-Prieto, M., Woldeyes, R. A., Fraser, J. S., Klein, M. L., Fiorin, G., and DeGrado, W. F. (2015) High-Resolution Structures of the M2 Channel from Influenza A Virus Reveal Dynamic Pathways for Proton Stabilization and Transduction. *Proc. Natl. Acad. Sci. U.S.A*. 112, 14260-14265
13. Williams, J., Zhang, Y., Schmidt-Rohr, K., and Hong, M. (2013) pH-Dependent Conformation, Dynamics, and Aromatic Interaction of the Gating Tryptophan Residue of the Influenza M2 Proton Channel from Solid-State NMR. *Biophys. J*. 104, 1698-1708
14. Cady, S., Schmidt-Rohr, K., Wang, J., Soto, C., DeGrado, W., and Hong, M. (2010) Structure of the Amantadine Binding Site of Influenza M2 Proton Channels in Lipid Bilayers. *Nature* 463, 689-692
15. Cady, S., Wang, J., Wu, Y., DeGrado, W., and Hong, M. (2011) Specific Binding of Adamantane Drugs and Direction of Their Polar Amines in the Pore of the Influenza M2 Transmembrane Domain in Lipid Bilayers and Dodecylphosphocholine Micelles Determined by NMR Spectroscopy. *J. Am. Chem. Soc*. 133, 4274-4284
16. Stouffer, A., Acharya, R., Salom, D., Levine, A., Di Costanzo, L., Soto, C., Tereshko, V., Nanda, V., Stayrook, S., and DeGrado, W. (2008) Structural Basis for the Function and Inhibition of an Influenza Virus Proton Channel. *Nature* 451, 596-599

17. Williams, J., Tietze, D., Wang, J., Wu, Y., DeGrado, W., and Hong, M. (2013) Drug-Induced Conformational and Dynamical Changes of the S31N Mutant of the Influenza M2 Proton Channel Investigated by Solid-State NMR. *J. Am. Chem. Soc.* 135, 9885-9897

18. Williams, J., Tietze, D., Lee, M., Wang, J., and Hong, M. (2016) Solid-State NMR Investigation of the Conformation, Proton Conduction, and Hydration of the Influenza B Virus M2 Transmembrane Proton Channel. *J. Am. Chem. Soc.* 138, 8143-8155

19. Wang, J., Pielak, R., McClintock, M., and Chou, J. (2009) Solution Structure and Functional Analysis of the Influenza B Proton Channel. *Nat. Struct. Mol. Biol.* 16, 1267-1271

20. Otomo, K., Toyama, A., Miura, T., and Takeuchi, H. (2009) Interactions Between Histidine and Tryptophan Residues in the BM2 Proton Channel from Influenza B Virus. *J. Biochem.* 145, 543-554

21. Ma, C., Soto, C., Ohigashi, Y., Taylor, A., Bournas, V., Glawe, B., Udo, M., DeGrado, W., Lamb, R., and Pinto, L. (2008) Identification of the Pore-Lining Residues of the BM2 Ion Channel Protein of Influenza B Virus. *J. Biol. Chem.* 283, 15921-15931

22. Hong, M., and DeGrado, W. F. (2012) Structural basis for proton conduction and inhibition by the influenza M2 protein. *Protein Sci.* 21, 1620-1633

23. Mould, J., Paterson, R., Takeda, M., Ohigashi, Y., Venkataraman, P., Lamb, R., and Pinto, L. (2003) Influenza B Virus BM2 Protein Has Ion Channel Activity that Conducts Protons Across Membranes. *Dev. Cell* 5, 175-184

24. Hong, M. (1999) Solid-State Dipolar INADEQUATE NMR Spectroscopy with a Large Double-Quantum Spectral Width. *J. Magn. Reson.* 136, 86-91

25. Hu, F., Schmidt-Rohr, K., and Hong, M. (2012) NMR Detection of pH-Dependent Histidine-Water Proton Exchange Reveals the Conduction Mechanism of a Transmembrane Proton Channel. *J. Am. Chem. Soc.* 134, 3703-3713

26. deAzevedo, E., Hu, W., Bonagamba, T., and Schmidt-Rohr, K. (1999) Centerband-Only Detection of Exchange: Efficient Analysis of Dynamics in Solids by NMR. *J. Am. Chem. Soc.* 121, 8411-8412

27. Schmidt-Rohr, K., deAzevedo, E., and Bonagamba, T. (2007) Centerband-Only Detection of Exchange (CODEX): Efficient NMR Analysis of Slow Motions in Solids. *eMagRes*

28. Goldberg, R., Kishore, N., and Lennen, R. (2002) Thermodynamic Quantities for the Ionization Reactions of Buffers. *J. Phys. Chem. Ref. Data* 31, 231-370

29. Luo, W., Mani, R., and Hong, M. (2007) Side-Chain Conformation of the M2 Transmembrane Peptide Proton Channel of Influenza A Virus from 19F Solid-State NMR. *J. Phys. Chem. B* 111, 10825-10832

30. Li, S., and Hong, M. (2011) Protonation, Tautomerization, and Rotameric Structure of Histidine: A Comprehensive Study by Magic-Angle-Spinning Solid-State NMR. *J. Am. Chem. Soc.* 133, 1534-1544

31. Takegoshi, K., Nakamura, S., and Terao, T. (2001) 13C-1H Dipolar-Assisted Rotational Resonance in Magic-Angle Spinning NMR. *Chem. Phys. Lett.* 344, 631-637

32. Hohwy, M., Rienstra, C., Jaroniec, C., and Griffin, R. (1999) Fivefold Symmetric Homonuclear Dipolar Recoupling in Rotating Solids: Application to Double Quantum Spectroscopy. *J. Chem. Phys.* 110, 7983-7992

33. Hong, M., and Griffin, R. (1998) Resonance Assignments for Solid Peptides by Dipolar-Mediated 13C/15N Correlation Solid-State NMR. *J. Am. Chem. Soc.* 120, 7113-7114

34. Luo, W., and Hong, M. (2006) Determination of the Oligomeric Number and Intermolecular Distances of Membrane Protein Assemblies by Anisotropic 1H-Driven Spin Diffusion NMR Spectroscopy. *J. Am. Chem. Soc.* 128, 7242-7251